Copper/Carbon Nanocomposites for Electrocatalytic Reduction of Oxygen to Hydrogen Peroxide

Bingzhe Yu,† John Diniz,† Kevin Lofgren, Qiming Liu, Rene Mercado, Forrest Nichols, Scott R. J. Oliver, and Shaowei Chen*

Read Online

ACCESS | Metrics & More | Article Recommendations | Supporting Information

ABSTRACT: Electrocatalytic synthesis of hydrogen peroxide (H_2O_2) via two-electron reduction of oxygen has emerged as an effective strategy to replace the traditional anthraquinone oxidation route. Herein, copper/carbon nanocomposites are prepared by pyrolytic treatment of a metal organic framework precursor, which consists of copper oxide (CuO_x) nanoparticles dispersed within a carbon matrix, as evidenced by results from transmission electron microscopy and X-ray photoelectron spectroscopy measurements. Deliberate electrochemical activation enriches the Cu_2O species on the nanocomposite surface and markedly enhances the performance of electrocatalytic oxygen reduction to H_2O_2 with the selectivity increased to 68% from ca. 45% (at +0.1 V) for the as-produced counterparts. This can be exploited for the effective electrochemical degradation of methylene blue. This is accounted for by the weakened interaction with peroxide intermediates on Cu_2O, as confirmed by results from first-principles calculations. Results from this study underline the significance of structural engineering based on electrochemical activation for the enhanced selectivity of oxygen reduction reaction for H_2O_2 production.

KEYWORDS: H_2O_2 generation, Two-electron oxygen reduction reaction, Copper oxide, Electrochemical activation
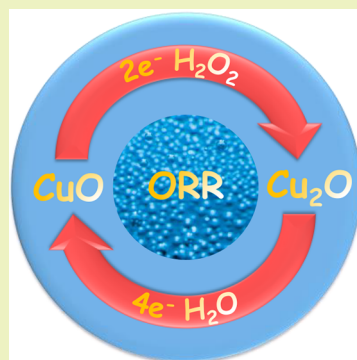
INTRODUCTION

Hydrogen peroxide (H_2O_2) is a critical commodity chemical that has found a diverse range of applications in, for instance, paper production, wastewater treatment, and oxidative disinfection.[1−5] Currently, industrial H_2O_2 production mainly relies on the energy-consuming anthraquinone process, leading to environmental issues because of its complicated synthesis steps and byproduct generation.[6,7] Additionally, safety risks arise during the transportation and storage processes because of the instability of concentrated H_2O_2.[8] Therefore, development of effective technologies for the on-site production of H_2O_2 has been attracting extensive interest, and two-electron ($2e^-$) electrochemical reduction of oxygen represents a unique strategy for H_2O_2 production.[4,9−12] Yet, this necessitates the rational design of high-performance catalysts that selectively power the $2e^-$ pathway of the oxygen reduction reaction (ORR), $O_2 + 2H^+ + 2e^- \rightarrow H_2O_2$, over the $4e^-$ route that produces H_2O instead, $O_2 + 4H^+ + 4e^- \rightarrow H_2O$.[13,14] In fact, the H_2O_2 selectivity can be regulated readily by the electrode catalysts, where the favorable electronic structure contributes to a reduced kinetic barrier for O_2 adsorption and preservation of the *OOH intermediate.[15,16] Mechanistically, this calls for a catalyst that favors a moderate adsorption of *OOH and avoids the breakage of the O−O bond in *OOH, which has been postulated as the determining step in the $2e^-$ ORR pathway for H_2O_2 generation.[17−19]

A range of electrocatalysts have been examined for H_2O_2 generation by $2e^-$ ORR, such as carbon-based materials,[4,20,21] noble metal alloys,[22] and nonprecious metal-based composites.[23,24] For example, Chen et al.[25] prepared oxygen-doped hierarchical porous carbon from resorcinol and p-phthalaldehyde and observed a H_2O_2 yield of 53.6%, due to the activation of the carbon scaffold by oxygen dopants and formation of a porous structure that facilitated mass transfer of reaction species. Lu et al.[26] reported that surface oxidation of carbon nanotubes (CNTs) via base treatment led to a selectivity of H_2O_2 production up to ca. 90%. In another study, Xia et al.[27] produced pure H_2O_2 solutions (up to 20%) at 90% selectivity via direct electrosynthesis in a solid electrolyte. Sun et al.[28] synthesized a series of metal−nitrogen−carbon (M−N−C) composites from zeolitic imidazolate framework-8 (ZIF-8) containing precursors and observed that the Co−N−C composite showed the highest selectivity (ca. 80%) in acidic media, where the binding energy of HO* was predicted to be near the peak of the volcano plot, whereas the selectivity of the Cu−N−C catalyst was much lower at only about 35%. Chang
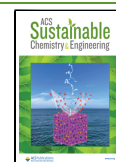
et al.[1] embedded partially oxidized palladium into defective multiwalled carbon nanotubes ($Pd^{\delta+}$-OCNT) by controlled pyrolysis, which achieved a selectivity for H_2O_2 generation over 95%, because of the interaction between the metal species and the oxidized carbon. Liu et al.[29] synthesized cobalt, nitrogen-codoped CNTs by controlled pyrolysis of ZIF-67 under an Ar/H_2 (10 vol %) atmosphere followed by acid leaching and obtained over 95% of H_2O_2 selectivity in acidic media, due to the deliberate engineering of the atomic configuration of the Co atomic centers dispersed within the N-doped carbon scaffold. Jiang et al.[30] prepared a range of transition metal-functionalized CNTs and obtained a H_2O_2 selectivity higher than 90% with Fe-CNT, which was ascribed to the formation of the Fe−C−O coordination moiety, in contrast to the Fe−C−N counterpart that is well-known for $4e^-$ ORR. Zhang et al.[31] synthesized N-doped hollow carbon polyhedra decorated with CoTe nanoparticles by pyrolysis of ZIF-67, which exhibited a H_2O_2 selectivity of 92.6%, as a consequence of the synergistic interaction between the CoTe nanoparticles and N-doped carbon scaffold.

Herein, $Cu_2(4,4'\text{-bipy})_2(O_3SCH_2CH_2SO_3)\cdot3H_2O$ (SLUG-22),[32] a copper-containing metal organic framework (MOF), was used as the precursor for the pyrolytic preparation of Cu/C nanocomposites. Electrochemical measurements showed that, upon deliberate electrochemical activation by rapid potential cycling, the Cu/C composites exhibited a remarkable enhancement of the H_2O_2 yield from ca. 45% to 68% (at +0.1 V) and, hence, effective electrochemical degradation of methylene blue. Spectroscopic measurements showed that potential cycling led to an apparent shift of the copper valence state from Cu^{2+} to Cu^+. The resultant Cu_2O species were most probably the active sites for the selective $2e^-$ pathway of ORR and responsible for the improved production of H_2O_2, as confirmed by results from first-principles calculations where Cu_2O exhibited a more favorable adsorption energy of *OOH (ΔG_{*OOH}) than CuO.

RESULTS AND DISCUSSION

SLUG-22, a Cu-containing MOF,[32] was synthesized by a facile hydrothermal procedure (Figure S1a), which was then pyrolytically converted into copper/carbon (Cu/C) nanocomposites at controlled temperatures, i.e., 600, 700, and 800 °C (Figure S1b). The resulting sample was referred to as Cu/C-600, Cu/C-700, and Cu/C-800, respectively. The experimental details are included in the Supporting Information. Notably, the resultant nanocomposites demonstrated an obvious electrocatalytic activity toward ORR in 0.1 M KOH (Figure S2). Figure 1a depicts the ORR polarization curves with a rotating ring-disk electrode (RRDE) of the Cu/C-600, Cu/C-700, and Cu/C-800 composites. One can see that, with the negative sweeping of the electrode potential, nonzero cathodic current started to appear, indicating apparent ORR activity of the Cu/C composites. Yet the ORR activity varied among the samples. In fact, one can see from the panel that the onset (E_{onset}) and half-wave potentials ($E_{1/2}$) were respectively estimated to be +0.691 and +0.477 V for Cu/C-600, +0.829 and +0.575 V for Cu/C-700, and +0.757 and +0.525 V for Cu/C-800; concurrently, the ring current density rose in the order of Cu/C-800 < Cu/C-600 < Cu/C-700. For example, the ring current density at +0.4 V was 0.116 mA cm^{-2} for Cu/C-800, 0.152 mA cm^{-2} for Cu/C-600, and 0.215 mA cm^{-2} for Cu/C-700. From Figure 1b, it can be seen that indeed the H_2O_2 yield (H_2O_2%, equation S1) increased in the order of Cu/C-800 <
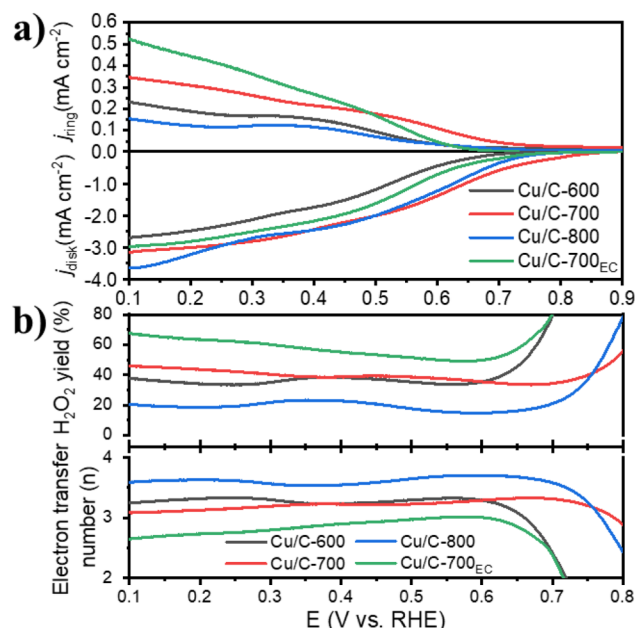

Figure 1. (a) RRDE ring (top) and disk (bottom) voltammograms of Cu/C nanocomposites prepared at different pyrolysis temperatures in oxygen-saturated 0.1 M KOH at the potential sweep rate of 10 mV·s^{-1} and rotation rate of 1600 rpm. (b) Combined plot of (upper left axis) the H_2O_2 yield and (lower left axis) electron transfer number (n) at different electrode potentials of the Cu/C sample series.

Cu/C-600 < Cu/C-700, and correspondingly, the number of electron transfer (n, equation S2) decreased in the reverse order. For instance, at +0.4 V, H_2O_2% = 22.7% and n = 3.55 for Cu/C-800, 38.1% and 3.24 for Cu/C-600, and 38.6% and 3.23 for Cu/C-700. These results suggest that 700 °C represented the optimal temperature to convert SLUG-22 to Cu/C nanocomposites in catalyzing the $2e^-$ oxygen reduction to H_2O_2 (45% at +0.1 V).

Interestingly, such a performance can be markedly enhanced by a deliberate electrochemical activation. From Figure 1a, one can see that after 10 000 potential cycles between +0.18 V and +0.98 V (the resulting sample was denoted as Cu/C-700$_{EC}$), whereas the disk limiting current remained virtually unchanged, $E_{1/2}$ shifted positively from +0.480 to +0.510 V and concurrently the ring current almost doubled, suggesting enhanced production of H_2O_2 (Figure 1a). Indeed, from Figure 1b, it can be seen that H_2O_2% increased markedly up to 68% within the potential range of +0.1 to +0.6 V, whereas n decreased to ca. 2.6. This suggests that structural engineering of the Cu/C composites occurred because of the electrochemical treatment and was responsible for the markedly enhanced selectivity of the $2e^-$ ORR pathway. Notably, the performance remained almost unvaried for up to 6 h of prolonged operation (Figure S3).

It should be noticed that when the Cu/C-700 sample was subject to acid leaching in HNO_3, the H_2O_2 yield diminished markedly to only 20−30% at +0.1 to +0.6 V (Figure S4). This suggests that the ORR activity was primarily attributable to the Cu species.

To understand the structural evolution of the Cu/C composites, the sample structures were first characterized and compared by transmission electron microscopy (TEM) measurements. From Figure 2a,b, it can be seen that Cu/C-700 exhibited a tendril-like structure, with dark-contrast
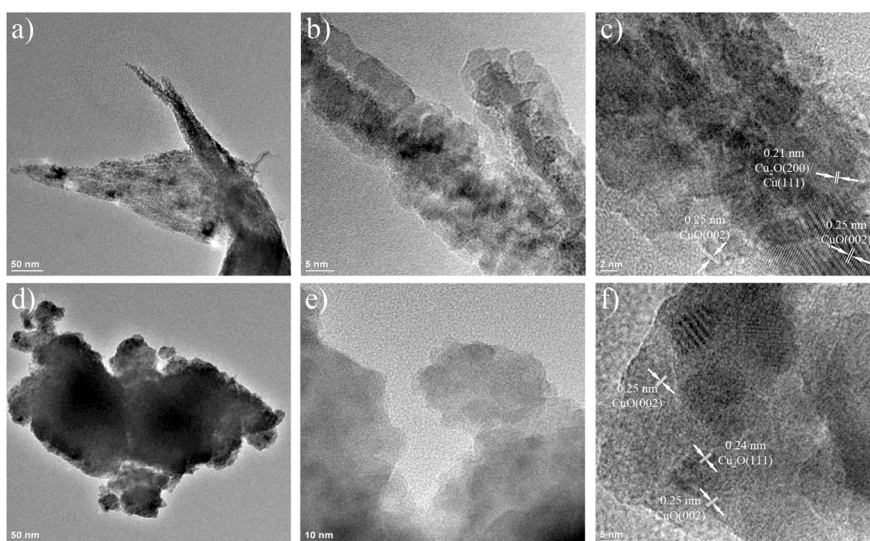
Figure 2. TEM images of (a–c) Cu/C-700 and (d–f) Cu/C-700$_{EC}$ at different magnifications. Scale bars are (a) 50 nm, (b) 5 nm, (c) 2 nm, (d) 50 nm, (e) 10 nm, and (f) 5 nm.

domains of a few tens of nanometers in length embedded within a flaky scaffold. In the high-resolution TEM measurements, the dark-contrast domains can be found to consist of nanocrystallites with clearly defined lattice fringes featuring interplanar distances of 0.21 and 0.25 nm (Figures 2c and S5). These can be ascribed to the (200) planes of Cu$_2$O (PDF 05-0667), (111) planes of Cu (PDF 04-0836), and (002) planes of CuO (PDF 45-0937), respectively, suggesting the formation of Cu, CuO, and Cu$_2$O species in the as-produced sample. Nanocrystalline Cu$_2$O and CuO can also be clearly resolved in the electrochemically activated Cu/C-700$_{EC}$ sample, as manifested in Figure 2d–f and Figure S6.

The Cu/C composite structures were further studied by X-ray diffraction (XRD) and Raman measurements. The XRD patterns are depicted in Figure S1b, where one can see that Cu/C-600, Cu/C-700, and Cu/C-800 all displayed three broad diffraction peaks (diamond shape) at 2θ = 36.3°, 41.6°, and 61.2° and three sharp ones (clover shape) at 43.3°, 50.4°, and 74.1°. The former can be ascribed to the (111), (200), and (220) facets of Cu$_2$O, whereas the latter are ascribed to the (111), (200), and (220) facets of Cu, respectively.[33,34] Note that no clearly defined XRD patterns could be resolved for CuO, likely due to the small crystalline domains (Figure 2). Consistent results were acquired in Raman measurements (Figure S7), where all Cu/C composites exhibited a D band (ca. 1350 cm$^-$) and a G band (ca. 1590 cm^{-1}), with a close intensity ratio (I_D/I_G) of ca. 1.0, suggesting successful graphitization of the MOF precursor. Additional vibrational bands can be resolved in the low wavenumber region, where the CuO A$_g$ mode can be identified at 284 cm^{-1} and B$_g$ modes at 335 and 617 cm^{-1}, whereas those at 150, 211, and 410 cm^{-1} are due to Cu$_2$O.[35−37]

Further structural insights were obtained in X-ray photoelectron spectroscopy (XPS) measurements. Figure S8a depicts the survey spectra, where the Cu 2p, O 1s, N 1s, C 1s, and S 2p electrons can be clearly resolved at ca. 932, 531, 400, 285, and 170 eV, respectively, for both Cu/C-700 and Cu/C-700$_{EC}$. Additionally, on the basis of the integrated peak areas, the elemental compositions of the samples were calculated to be 72.73 at % C, 20.83 at % O, 3.07 at % N, 2.04 at % Cu, and 1.33 at % S in Cu/C-700 (Table S1). Of

note is that the Cu content (2.04 at %, 9.12 wt %) is lower than that obtained from ICP-OES measurements (23.4 wt %). This is likely because XPS probes mostly the top surface layers of the samples, and part of the Cu species was encapsulated within a carbon layer for the Cu/C composites (Figure 2). In addition, no Cu species was detectable beyond the instrument baseline in the electrolyte solution after potential cycling of the Cu/C-700 sample, suggesting essentially no loss of Cu from the catalysts during electrochemical activation.

The high-resolution XPS spectra of the C 1s, N 1s, and S 2p electrons are shown in Figures S9−S11, and the results corroborate the successful transformation of the MOF precursor into nitrogen- and sulfur-doped carbon. The high-resolution spectra of the Cu 2p electrons are shown in Figure 3a. Deconvolution yields two peaks at 932.6 and 934.4 eV for the Cu/C-700 sample, which can be ascribed to the 2p$_{3/2}$ electrons of Cu/Cu$^+$ and Cu^{2+}, respectively, and two Cu^{2+} satellite peaks at 941.8 and 944.2 eV.[38,39] Similar results were obtained with the Cu/C-700$_{EC}$ sample; yet the binding energies of the Cu/Cu$^+$ and Cu^{2+} 2p$_{3/2}$ electrons increased somewhat to 932.8 and 935.3 eV, suggesting the formation of increasingly electron-deficient Cu species after electrochemical activation. Interestingly, from the integrated peak areas, it can be seen that the Cu/Cu$^+$:Cu^{2+} atomic ratio actually increased by almost threefold to 0.29 for Cu/C-700$_{EC}$ from 0.10 for Cu/C-700. This suggests enrichment of the Cu$^+$ species after electrochemical treatment.[40]

Note that whereas the 2p binding energies of Cu and Cu$^+$ are almost indistinguishable, their LMM Auger positions are markedly different, which can be exploited to differentiate their compositions. From the spectra in Figure 3b, one can see that the Cu/C-700 and Cu/C-700$_{EC}$ samples indeed contained Cu (567.9 eV), Cu$^+$ (570.1 eV), and Cu^{2+} (569.0 eV) species.[41,42] On the basis of the integrated peak areas, it can be seen that Cu$^+$ accounts for about 6.62% of the total Cu content in Cu/C-700 and increased by over twofold to 14.0% in Cu/C-700$_{EC}$.

Consistent results were obtained from the O 1s spectra. From Figure 3c, the Cu/C-700 sample can be observed to include a peak at 530.0 eV, due to oxygen in metal oxides (i.e., O−Cu),[43] consistent with results from TEM measurements that the CuO and Cu$_2$O species were formed in the sample
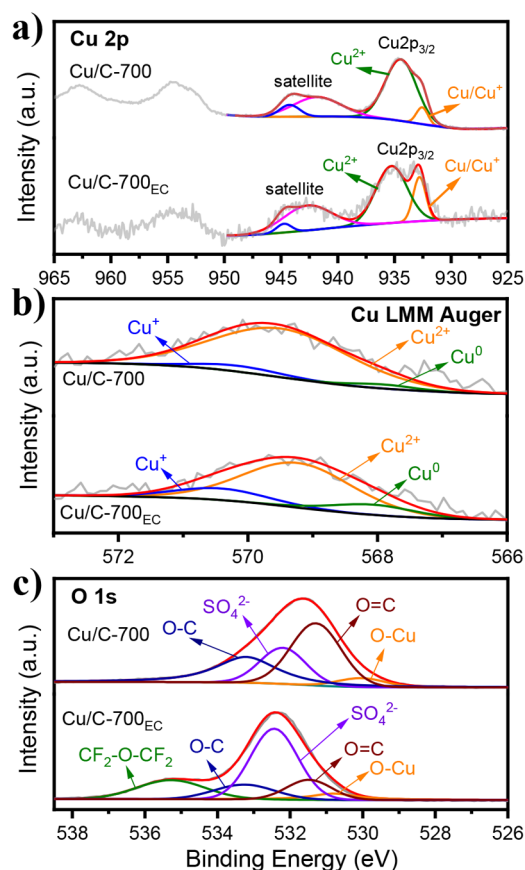
Figure 3. High-resolution XPS scans of the (a) Cu 2p, (b) Cu LMM Auger, and (c) O 1s electrons of Cu/C-700 and Cu/C-700$_{EC}$. Gray curves are raw data and colored curves are deconvolution fits.

(additional components at 531.3, 532.2, and 533.2 eV are due to O=C, SO$_4^{2-}$, and O−C, respectively).[44−46] Interestingly, for the Cu/C-700$_{EC}$ sample, whereas the O=C, SO$_4^{2-}$, and O−C peaks remained virtually unchanged (with an additional peak at 535.4 eV corresponding to CF$_2$−O−CF$_2$ of residual Nafion), the O−Cu peak actually shifted to a markedly higher binding energy (530.8 eV), again, confirming the formation of electron-deficient copper oxides.[43,47,48] Taken together, these results suggest that electrochemical activation led to effective enrichment of the Cu$_2$O species on the nanocomposite surface.[49] As Cu$_2$O is far more active than CuO in catalyzing the 2e$^-$ ORR (Figure S12), the observed structural evolution is in excellent agreement with the enhanced selectivity of H$_2$O$_2$ production with Cu/C-700$_{EC}$, as compared to Cu/C-700.[50−52] This can also account for the best ORR performance of Cu/C-700 among the three as-produced samples, as it possessed the highest Cu$^+$ concentration of 0.61 at %, in comparison to 0.35 at % for Cu/C-600 and 0.21 at % for Cu/C-800 (Figures S8b, S13, and S14 and Table S1).

The selective production of H$_2$O$_2$ can be exploited for the on-site degradation of organic dye pollutants, e.g., methylene blue (MB, experimental details in the Supporting Information). Experimentally, the electrode potential was fixed at +0.2 V in a solution containing 25 mg L^{-1} MB and 0.1 M KOH. One can see that the characteristic adsorption peak of MB at 664 nm decreased in intensity with increasing reaction time with both Cu/C-700 and Cu/C-700$_{EC}$ (Figure 4a,b), confirming effective degradation of MB by the electrochemically produced H$_2$O$_2$.
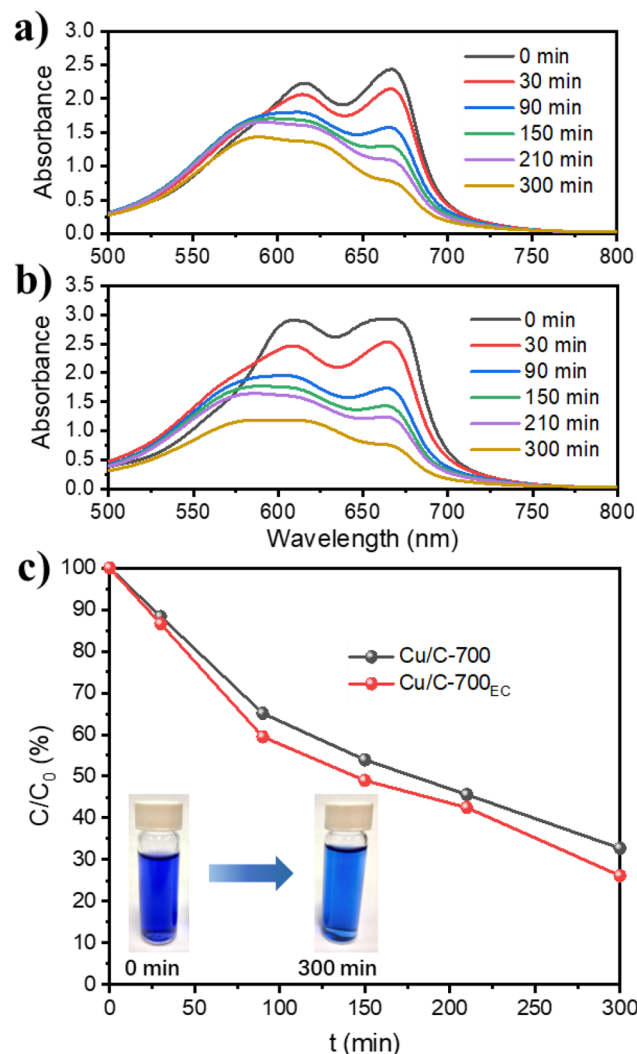
Figure 4. UV−vis absorption spectra of methyl blue (25 mg L^{-1}) at different electrolytic times in 0.1 M KOH with (a) Cu/C-700 and (b) Cu/C-700$_{EC}$. (c) Concentration of MB over time on Cu/C-700 and Cu/C-700$_{EC}$. Insets are the photographs of the MB solution at 0 and 300 min of reaction time with Cu/C-700$_{EC}$.

In fact, the deep blue color of the MB solution faded apparently after 300 min of reaction (Figure 4c inset), with a degradation efficiency of 67.3% for Cu/C-700 and somewhat better at 73.9% for Cu/C-700$_{EC}$ (Figure 4c), corresponding to the production of 2.40 mg mL^{-1} H$_2$O$_2$ for the former and 2.99 mg mL^{-1} for the latter (Figure S15 and Table S2). This is consistent with the ORR performance described above.

First-principles computation was then carried out to unravel the mechanistic insights (computational details in the Supporting Information). It has been shown that the key intermediate of 2e$^-$ ORR is the OOH species, as too strong or too weak adsorption on the active sites would lead to either the 4e$^-$ pathway to water or low activity.[30] Therefore, the adsorption free energy (ΔG_{*OOH}) was exploited as the descriptor to examine the electrocatalytic activity of the Cu/C composites. On the basis of the results from experimental measurements (Figure 2), the (111) facets of CuO and Cu$_2$O were used as the structural models, and the adsorption of OOH on the surfaces was analyzed and compared. From Figure 5a,b, one can find that the Cu−O$_{OOH}$ bond length was
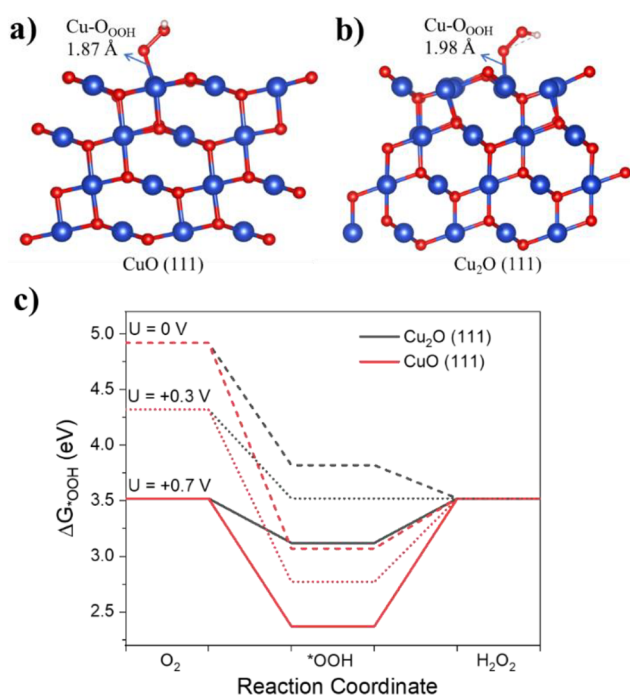
Figure 5. Computational study of OOH adsorption on CuO (111) and Cu$_2$O (111). Relaxed models of (a) *OOH CuO (111) and (b) *OOH Cu$_2$O (111). (c) Gibbs free energy of the adsorption of OOH intermediates on Cu$_2$O (111) and CuO (111) at different potentials (U) in 2e$^-$ ORR.

1.87 Å on CuO and elongated to 1.98 Å on Cu$_2$O, implying a weakened adsorption of the OOH intermediate on the latter. This was also reflected by the corresponding adsorption free energy. As depicted in Figure 5c, at the theoretical onset potential of 2e$^-$ ORR (+0.7 V), ΔG_{*OOH} was estimated to be 2.37 eV on CuO and 3.12 eV on Cu$_2$O, denoting that the potential limiting step (PDS) was the desorption of OOH on both surfaces. In comparison to the ideal ΔG_{*OOH} of 3.52 eV,[53] the energy barrier was estimated to be 1.15 eV on CuO and diminished markedly to only 0.40 eV on Cu$_2$O.

Additionally, from Figure 5c, one can observe that at the lower biased potentials of U = +0.3 and 0 V, the production of H$_2$O$_2$ can occur spontaneously on Cu$_2$O, whereas the reaction remains energetically unfavorable on CuO. Such a discrepancy of the activity can also be interpreted by their different electronic configurations, where Cu$_2$O possesses a closed 3d^{10} shell while CuO exhibits an unfilled 3d^9 shell,[54] such that a weaker interaction with OOH species is expected with the former. This is conducive to the 2e$^-$ ORR pathway, as manifested in the above experimental measurements.

CONCLUSIONS

In this study, Cu/C composites were prepared pyrolytically from a MOF precursor, with CuO$_x$ species embedded within a carbon scaffold. In electrochemical studies, the composites exhibited apparent electrocatalytic activity toward the 2e$^-$ ORR, and the selectivity was markedly enhanced after electrochemical activation by potential cycling at a fast scan rate, due to the surface enrichment of the Cu$_2$O species. This was confirmed by results from first-principles calculations. Such a unique feature could be exploited for the electrochemical production of H$_2$O$_2$ for the degradation of organic dye pollutants. Results from this study underscore the fundamental significance of structural engineering in the regulation of the electrocatalytic activity and selectivity of functional nanocomposites.

ASSOCIATED CONTENT

Supporting Information

The Supporting Information is available free of charge at https://pubs.acs.org/doi/10.1021/acssuschemeng.2c04746.

Additional experimental details and data. Experimental procedures; XRD patterns; cyclic voltammograms; stability test of Cu/C-700$_{EC}$; TEM lattice fringes and interplanar spacings; Raman spectra; XPS full spectra, high-resolution scans of C 1s, N 1s, and S 2p electrons, and Cu LMM Auger spectra; ORR tests of commercial Cu$_2$O and CuO; calibration of H$_2$O$_2$ degradation of methylene blue; and summary of elemental composition and H$_2$O$_2$ yield (PDF)

AUTHOR INFORMATION

Corresponding Author

Shaowei Chen − *Department of Chemistry and Biochemistry, University of California, Santa Cruz, California 95064, United States;* ⊙ orcid.org/0000-0002-3668-8551; Email: shaowei@ucsc.edu

Authors

Bingzhe Yu − *Department of Chemistry and Biochemistry, University of California, Santa Cruz, California 95064, United States*

John Diniz − *Department of Chemistry and Biochemistry, University of California, Santa Cruz, California 95064, United States*

Kevin Lofgren − *Department of Chemistry and Biochemistry, University of California, Santa Cruz, California 95064, United States*

Qiming Liu − *Department of Chemistry and Biochemistry, University of California, Santa Cruz, California 95064, United States;* ⊙ orcid.org/0000-0001-5839-5453

Rene Mercado − *Department of Chemistry and Biochemistry, University of California, Santa Cruz, California 95064, United States*

Forrest Nichols − *Department of Chemistry and Biochemistry, University of California, Santa Cruz, California 95064, United States*

Scott R. J. Oliver − *Department of Chemistry and Biochemistry, University of California, Santa Cruz, California 95064, United States;* ⊙ orcid.org/0000-0002-6160-1518

Complete contact information is available at: https://pubs.acs.org/10.1021/acssuschemeng.2c04746

■ REFERENCES

(1) Chang, Q. W.; Zhang, P.; Mostaghimi, A. H. B.; Zhao, X. R.; Denny, S. R.; Lee, J. H.; Gao, H. P.; Zhang, Y.; Xin, H. L. L.; Siahrostami, S.; et al. Promoting H_2O_2 production via 2-electron oxygen reduction by coordinating partially oxidized Pd with defect carbon. *Nat. Commun.* 2020, 11 (1), 2178.

(2) Fukuzumi, S.; Yamada, Y.; Karlin, K. D. Hydrogen peroxide as a sustainable energy carrier: Electrocatalytic production of hydrogen peroxide and the fuel cell. *Electrochim. Acta* 2012, 82, 493−511.

(3) Goti, A.; Cardona, F. Hydrogen peroxide in green oxidation reactions: Recent catalytic processes. *Nato Sci. Peace Secur* 2008, 191−212.

(4) Hu, Y. Z.; Zhang, J. J.; Shen, T.; Li, Z. R.; Chen, K.; Lu, Y.; Zhang, J.; Wang, D. L. Efficient Electrochemical Production of H2O2 on Hollow N-Doped Carbon Nanospheres with Abundant Micropores. *ACS Appl. Mater. Interfaces* 2021, 13 (25), 29551−29557.

(5) Nichols, F.; Ozoemena, K. I.; Chen, S. W. Electrocatalytic Generation of Reactive Species and Implications in Microbial Inactivation. *Chin. J. Catal.* 2022, 43 (6), 1399−1416.

(6) Campos-Martin, J. M.; Blanco-Brieva, G.; Fierro, J. L. Hydrogen peroxide synthesis: an outlook beyond the anthraquinone process. *Angew. Chem., Int. Ed.* 2006, 45 (42), 6962−6984.

(7) Yang, S.; Verdaguer-Casadevall, A.; Arnarson, L.; Silvioli, L.; Colic, V.; Frydendal, R.; Rossmeisl, J.; Chorkendorff, I.; Stephens, I. E. L. Toward the Decentralized Electrochemical Production of H_2O_2: A Focus on the Catalysis. *ACS Catal.* 2018, 8 (5), 4064−4081.

(8) Jiang, Y. Y.; Ni, P. J.; Chen, C. X.; Lu, Y. Z.; Yang, P.; Kong, B.; Fisher, A.; Wang, X. Selective Electrochemical H_2O_2 Production through Two-Electron Oxygen Electrochemistry. *Adv. Energy Mater.* 2018, 8 (31), 1801909.

(9) Xiao, X.; Wang, T. J.; Bai, J.; Li, F. M.; Ma, T. Y.; Chen, Y. Enhancing the Selectivity of H_2O_2 Electrogeneration by Steric Hindrance Effect. *ACS Appl. Mater. Interfaces* 2018, 10 (49), 42534−42541.

(10) Zhu, W. Y.; Chen, S. W. Recent Progress of Single-Atom Catalysts in the Electrocatalytic Reduction of Oxygen to Hydrogen Peroxide. *Electroanalysis* 2020, 32 (12), 2591−2602.

(11) Zhang, Q. Z.; Zhou, M. H.; Ren, G. B.; Li, Y. W.; Li, Y. C.; Du, X. D. Highly efficient electrosynthesis of hydrogen peroxide on a superhydrophobic three-phase interface by natural air diffusion. *Nat. Commun.* 2020, 11 (1), 1731.

(12) Zhang, X.; Zhao, X. H.; Zhu, P.; Adler, Z.; Wu, Z. Y.; Liu, Y. Y.; Wang, H. T. Electrochemical oxygen reduction to hydrogen peroxide at practical rates in strong acidic media. *Nat. Commun.* 2022, 13 (1), 2880.

(13) Chen, D.; Sun, P. C.; Liu, H.; Yang, J. Bimetallic Cu-Pd alloy multipods and their highly electrocatalytic performance for formic acid oxidation and oxygen reduction. *J. Mater. Chem. A* 2017, 5 (9), 4421−4429.

(14) Wang, W.; Hu, Y. C.; Liu, Y. C.; Zheng, Z. Y.; Chen, S. L. Self-Powered and Highly Efficient Production of H_2O_2 through a Zn-Air Battery with Oxygenated Carbon Electrocatalyst. *ACS Appl. Mater. Interfaces* 2018, 10 (38), 31855−31859.

(15) Pang, Y. Y.; Xie, H.; Sun, Y.; Titirici, M. M.; Chai, G. L. Electrochemical oxygen reduction for H_2O_2 production: catalysts, pH effects and mechanisms. *J. Mater. Chem. A* 2020, 8 (47), 24996−25016.

(16) Wang, N.; Ma, S. B.; Zuo, P. J.; Duan, J. Z.; Hou, B. R. Recent Progress of Electrochemical Production of Hydrogen Peroxide by Two-Electron Oxygen Reduction Reaction. *Adv. Sci.* 2021, 8 (15), 2100076.

(17) Seh, Z. W.; Kibsgaard, J.; Dickens, C. F.; Chorkendorff, I. B.; Norskov, J. K.; Jaramillo, T. F. Combining theory and experiment in electrocatalysis: Insights into materials design. *Science* 2017, 355 (6321), eaad4998.

(18) Woo, J.; Lim, J. S.; Kim, J. H.; Joo, S. H. Heteroatom-doped carbon-based oxygen reduction electrocatalysts with tailored four-electron and two-electron selectivity. *Chem. Commun.* 2021, 57 (60), 7350−7361.

(19) Zhao, H.; Yuan, Z. Y. Design Strategies of Non-Noble Metal-Based Electrocatalysts for Two-Electron Oxygen Reduction to Hydrogen Peroxide. *ChemSusChem* 2021, 14 (7), 1616−1633.

(20) Liu, Y. M.; Quan, X.; Fan, X. F.; Wang, H.; Chen, S. High-Yield Electrosynthesis of Hydrogen Peroxide from Oxygen Reduction by Hierarchically Porous Carbon. *Angew. Chem., Int. Ed.* 2015, 54 (23), 6837−6841.

(21) Jia, N.; Yang, T.; Shi, S. F.; Chen, X. B.; An, Z. W.; Chen, Y.; Yin, S. W.; Chen, P. N,F-Codoped Carbon Nanocages: An Efficient Electrocatalyst for Hydrogen Peroxide Electroproduction in Alkaline and Acidic Solutions. *ACS Sustain. Chem. Eng.* 2020, 8 (7), 2883−2891.

(22) Ko, Y. J.; Choi, K.; Yang, B.; Lee, W. H.; Kim, J. Y.; Choi, J. W.; Chae, K. H.; Lee, J. H.; Hwang, Y. J.; Min, B. K.; et al. A catalyst design for selective electrochemical reactions: direct production of hydrogen peroxide in advanced electrochemical oxidation. *J. Mater. Chem. A* 2020, 8 (19), 9859−9870.

(23) Lin, Z. H.; Zhang, Q. R.; Pan, J.; Tsounis, C.; Esmailpour, A. A.; Xi, S. B.; Yang, H. Y.; Han, Z. J.; Yun, J.; Amal, R.; et al. Atomic Co decorated free-standing graphene electrode assembly for efficient hydrogen peroxide production in acid. *Energy Environ. Sci.* 2022, 15, 1172.

(24) Xu, H.; Zhang, S. B.; Geng, J.; Wang, G. Z.; Zhang, H. M. Cobalt single atom catalysts for the efficient electrosynthesis of hydrogen peroxide. *Inorg. Chem. Front* 2021, 8 (11), 2829−2834.

(25) Chen, Z. X.; Li, Y. Z.; Wu, M.; Cao, Y. L. Oxygen-Doped Hierarchical Porous Carbon with Improved Selectivity of Hydrogen Peroxide in an Oxygen Reduction Reaction. *Energy Fuel* 2021, 35 (3), 2665−2673.

(26) Lu, Z. Y.; Chen, G. X.; Siahrostami, S.; Chen, Z. H.; Liu, K.; Xie, J.; Liao, L.; Wu, T.; Lin, D. C.; Liu, Y. Y.; et al. High-efficiency oxygen reduction to hydrogen peroxide catalysed by oxidized carbon materials. *Nat. Catal* 2018, 1 (2), 156−162.

(27) Xia, C.; Xia, Y.; Zhu, P.; Fan, L.; Wang, H. T. Direct electrosynthesis of pure aqueous H_2O_2 solutions up to 20% by weight using a solid electrolyte. *Science* 2019, 366 (6462), 226.

(28) Sun, Y. Y.; Silvioli, L.; Sahraie, N. R.; Ju, W.; Li, J. K.; Zitolo, A.; Li, S.; Bagger, A.; Arnarson, L.; Wang, X. L.; et al. Activity-Selectivity Trends in the Electrochemical Production of Hydrogen Peroxide over Single-Site Metal-Nitrogen-Carbon Catalysts. *J. Am. Chem. Soc.* 2019, 141 (31), 12372−12381.

(29) Liu, W.; Zhang, C.; Zhang, J.; Huang, X.; Song, M.; Li, J.; He, F.; Yang, H.; Zhang, J.; Wang, D. Tuning the atomic configuration of Co-N-C electrocatalyst enables highly-selective H_2O_2 production in acidic media. *Appl. Catal. B: Environ.* 2022, 310, 121312.

(30) Jiang, K.; Back, S.; Akey, A. J.; Xia, C.; Hu, Y. F.; Liang, W. T.; Schaak, D.; Stavitski, E.; Norskov, J. K.; Siahrostami, S.; et al. Highly selective oxygen reduction to hydrogen peroxide on transition metal single atom coordination. *Nat. Commun.* 2019, 10, 3997.

(31) Zhang, L. C.; Liang, J.; Yue, L. C.; Dong, K.; Xu, Z. Q.; Li, T. S.; Liu, Q.; Luo, Y. L.; Liu, Y.; Gao, S. Y.; et al. CoTe nanoparticle-embedded N-doped hollow carbon polyhedron: an efficient catalyst for H_2O_2 electrosynthesis in acidic media. *J. Mater. Chem. A* 2021, 9 (38), 21703−21707.

(32) Fei, H. H.; Rogow, D. L.; Oliver, S. R. J. Reversible Anion Exchange and Catalytic Properties of Two Cationic Metal-Organic Frameworks Based on Cu(I) and Ag(I). *J. Am. Chem. Soc.* **2010**, *132* (20), 7202−7209.

(33) Lee, Y.; Choi, J. R.; Lee, K. J.; Stott, N. E.; Kim, D. Large-scale synthesis of copper nanoparticles by chemically controlled reduction for applications of inkjet-printed electronics. *Nanotechnology* **2008**, *19* (41), 415604.

(34) Kim, H. S.; Kumar, M. D.; Park, W. H.; Patel, M.; Kim, J. Cu_4O_3-based all metal oxides for transparent photodetectors. *Sensor Actuat a-Phys.* **2017**, *253*, 35−40.

(35) Xu, J. F.; Ji, W.; Shen, Z. X.; Li, W. S.; Tang, S. H.; Ye, X. R.; Jia, D. Z.; Xin, X. Q. Raman spectra of CuO nanocrystals. *J. Raman Spectrosc.* **1999**, *30* (5), 413−415.

(36) Lu, C. L.; Li, Z. P.; Ren, L. W.; Su, N.; Lu, D. N.; Liu, Z. In Situ Oxidation of Cu_2O Crystal for Electrochemical Detection of Glucose. *Sensors-Basel* **2019**, *19* (13), 2926.

(37) Zhang, L.; Hu, J. S.; Pan, C. L.; Huang, X. H.; Hou, C. M. Morphology-controllable synthesis of novel $Bi_{25}VO_{40}$ microcubes: optical properties and catalytic activities for the reduction of aromatic nitro compounds. *RSC Adv.* **2015**, *5* (96), 78457−78467.

(38) Gao, Y. J.; Yang, F. Y.; Yu, Q. H.; Fan, R.; Yang, M.; Rao, S. Q.; Lan, Q. C.; Yang, Z. J.; Yang, Z. Q. Three-dimensional porous Cu@Cu_2O aerogels for direct voltammetric sensing of glucose. *Microchim Acta* **2019**, *186* (3), 192.

(39) Liu, K.; Song, Y.; Chen, S. W. Oxygen reduction catalyzed by nanocomposites based on graphene quantum dots-supported copper nanoparticles. *Int. J. Hydrogen Energy* **2016**, *41* (3), 1559−1567.

(40) Akhavan, O.; Azimirad, R.; Safa, S.; Hasani, E. CuO/$Cu(OH)_2$ hierarchical nanostructures as bactericidal photocatalysts. *J. Mater. Chem.* **2011**, *21* (26), 9634−9640.

(41) Biesinger, M. C. Advanced analysis of copper X-ray photoelectron spectra. *Surf. Interface Anal.* **2017**, *49* (13), 1325−1334.

(42) Martin, L.; Martinez, H.; Poinot, D.; Pecquenard, B.; Le Cras, F. Comprehensive X-ray Photoelectron Spectroscopy Study of the Conversion Reaction Mechanism of CuO in Lithiated Thin Film Electrodes. *J. Phys. Chem. C* **2013**, *117* (9), 4421−4430.

(43) Dan, Z. H.; Yang, Y. L.; Qin, F. X.; Wang, H.; Chang, H. Facile Fabrication of Cu_2O Nanobelts in Ethanol on Nanoporous Cu and their Photodegradation of Methyl Orange. *Materials* **2018**, *11* (3), 446.

(44) Chulliyote, R.; Hareendrakrishnakumar, H.; Raja, M.; Gladis, J. M.; Stephan, A. M. Sulfur-Immobilized Nitrogen and Oxygen Co-Doped Hierarchically Porous Biomass Carbon for Lithium-Sulfur Batteries: Influence of Sulfur Content and Distribution on Its Performance. *Chemistryselect* **2017**, *2* (32), 10484−10495.

(45) Zhang, Y. P.; Dong, K. T.; Liu, Z.; Wang, H. L.; Ma, S. X.; Zhang, A. Y.; Li, M.; Yu, L. Q.; Li, Y. Sulfurized hematite for photo-Fenton catalysis. *Prog. Nat. Sci-Mater.* **2017**, *27* (4), 443−451.

(46) Kwan, Y. C. G.; Ng, G. M.; Huan, C. H. A. Identification of functional groups and determination of carboxyl formation temperature in graphene oxide using the XPS O 1s spectrum. *Thin Solid Films* **2015**, *590*, 40−48.

(47) Wang, Y. T.; Lu, Y. Y.; Zhan, W. W.; Xie, Z. X.; Kuang, Q.; Zheng, L. S. Synthesis of porous Cu_2O/CuO cages using Cu-based metal-organic frameworks as templates and their gas-sensing properties. *J. Mater. Chem. A* **2015**, *3* (24), 12796−12803.

(48) Han, J.; Chang, J.; Wei, R.; Ning, X. H.; Li, J.; Li, Z. X.; Guo, H. L.; Yang, Y. Mechanistic investigation on tuning the conductivity type of cuprous oxide (Cu_2O) thin films via deposition potential. *Int. J. Hydrogen Energy* **2018**, *43* (30), 13764−13777.

(49) Fan, H. H.; Weng, W. L.; Lee, C. Y.; Liao, C. N. Electrochemical Cycling-Induced Spiky Cu_xO/Cu Nanowire Array for Glucose Sensing. *Acs Omega* **2019**, *4* (7), 12222−12229.

(50) Putra, R. P.; Samejima, Y.; Nakabayashi, S.; Horino, H.; Rzeznicka, I. I. Copper-based electrocatalyst derived from a copper chelate polymer for oxygen reduction reaction in alkaline solutions. *Catal. Today* **2022**, *388−389*, 360−364.

(51) Xiao, H.; Li, B.; Zhao, M.; Li, Y.; Hu, T. J.; Jia, J. F.; Wu, H. S. Electrosynthesized CuO_x/graphene by a four-electrode electrolysis system for the oxygen reduction reaction to hydrogen peroxide. *Chem. Commun.* **2021**, *57* (34), 4118−4121.

(52) Jain, P.; Jha, S.; Ingole, P. P. Strong metal-support interaction in copper hexacyanoferrate nanocube decorated functionalized multiwall carbon nanotubes for enhanced bi-functional oxygen electrocatalytic activity and stability. *Sustain Energy Fuels* **2022**, *6* (4), 1094−1107.

(53) Zhao, X.; Yin, Q.; Mao, X.; Cheng, C.; Zhang, L.; Wang, L.; Liu, T. F.; Li, Y.; Li, Y. Theory-guided design of hydrogen-bonded cobaltoporphyrin frameworks for highly selective electrochemical H_2O_2 production in acid. *Nat. Commun.* **2022**, *13* (1), 2721.

(54) Pauly, N.; Tougaard, S.; Yubero, F. Determination of the Cu 2p primary excitation spectra for Cu, Cu_2O and CuO. *Surf. Sci.* **2014**, *620*, 17−22.

⧉ Recommended by ACS